



Recognition of immunogold markers in electron micrographs

Ruixuan Wang^a, Himanshu Pokhariya^a, Stephen J. McKenna^a, John Lucocq^{b,*}

^aSchool of Computing, University of Dundee, Dundee DD1 4HN, UK

^bDivision of Cell Biology and Immunology, College of Life Sciences, University of Dundee, Dundee DD1 5EH, UK

ARTICLE INFO

Article history:

Received 4 March 2011

Received in revised form 3 June 2011

Accepted 12 July 2011

Available online 26 July 2011

Keywords:

Immunolectron microscopy

Immunogold markers

Spot

ABSTRACT

Immunolectron microscopy is used in cell biological research to study the spatial distribution of intracellular macromolecules at the ultrastructural level. Colloidal gold particles (immunogold markers) are commonly used to localise molecules of interest on ultrathin sections and can be visualised in transmission electron micrographs as dark spots. Quantitative analysis involves detection of the immunogold markers, and is often performed manually or interactively as part of a stereological estimation technique. The method presented in this paper automatically detects and counts immunogold markers, estimating the location, size and type of each marker. It was evaluated on single-labelled as well as double-labelled images showing markers of two different sizes. This is a first step towards automatic analysis of immunolectron micrographs, enabling a rapid and more complete quantitative analysis than is currently practicable.

© 2011 Elsevier Inc. All rights reserved.

1. Introduction

Immunolectron microscopy is a powerful tool used for studying the spatial distribution of macromolecules at the ultrastructural level. A common approach is to label ultrathin sections that contain protein antigens using antibodies whose locations can be highlighted using electron dense microscopic markers such as colloidal gold (Webster et al., 2008; Lucocq, 2008). Most often antibodies act as primary affinity reagents that bind to the antigens (the molecules of interest) and these are then localised using secondary (second step) affinity reagents complexed to the gold particles. Such immunogold markers are relatively easily visualised in transmission electron micrographs because of the electron density of the gold particles. The particles are elemental crystals of gold that appear approximately spherical by transmission electron microscopy and appear as relatively dark spots against the cellular background after images have been recorded (see Fig. 1 for a well contrasted example). A further application of this technology provides co-localisation of multiple antigens by using immunogold markers of different sizes to mark the locations of the different antibodies, and therefore the antigens. This approach can be used to study the possible functional relationships between macromolecules as well as their localisation relative to various intracellular compartments.

The particulate nature of the colloidal gold particles opens up the possibility of quantifying the label by counting procedures.

The relative number of gold particles associated with cell compartments or structures (distribution) and the concentration (density) over structure profiles are useful measures that report important information about the target antigen. Accordingly a portfolio of quantitative methods, based on established sampling strategies and stereological estimators, has now been developed. These methods allow minimally biased estimation of particle distribution and particle densities and provide statistical techniques for evaluating the results (Mayhew, 2007; Mayhew et al., 2002; Lucocq, 1994, 2008; Lucocq et al., 2004; Lucocq and Gawden-Bone, 2009, 2010). The starting point for these and many other quantitative analyses is the detection of immunogold markers in electron micrographs. Detection and counting are almost always carried out by the experimenter but this can be a tedious and labour-intensive task. It not only requires training but also can be error-prone (Monteiro-Leal et al., 2003).

A few methods for automatic or semi-automatic detection of immunogold markers have been reported. An early method applied morphological operations and interactive threshold selection to segment markers of fixed size (Lebonvallet et al., 1991). Brandt et al. (2001) modelling the appearance of a gold marker as a Gaussian-blurred circular region with fixed radius. They used template matching and hysteresis thresholding for marker detection. Detected regions with low circularity were removed to reduce the false positive rate. However in preliminary experiments for this study we have found that whilst fine-tuning of thresholds could produce reasonable results on one region of an image, poor detection tended to occur elsewhere even within the same image using this method. Finally, Monteiro-Leal et al. (2003) used simple grey level thresholding with user-selected threshold values to obtain

* Corresponding author. Address: Medical and Biological Sciences Building, University of St. Andrews, North Haugh, St. Andrews, Fife KY16 9TF, UK.

E-mail address: jml7@st-andrews.ac.uk (J. Lucocq).

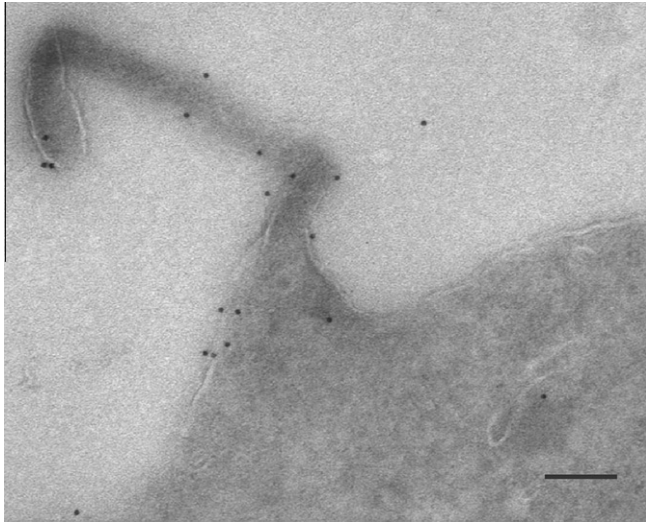


Fig.1. A well contrasted region of an immunoelectron micrograph in which cell (mid-grey), background (light grey) and 10 nm diameter immunogold markers (punctate, dark grey) are clearly distinguishable. Thawed ultrathin cryosection contrasted using uranyl acetate/methylcellulose. Bar, 100 nm.

foreground regions, which were then classified based on their shape and size as small particle, large particle, or cluster of particles. This method assumed that pixels at immunogold markers were darker than anything else in the images. However, images in which markers are very highly contrasted are often obtained at the expense of loss of intracellular structure information.

The method presented in this paper automatically detects and counts immunogold markers, estimating the location, size and type of each marker. We have evaluated the method using images showing immunogold markers of similar size (single labelling) as well as using markers of two different sizes (double labelling) marking different molecular components.

2. Method

2.1. Overview

The work reported here started with a search, which utilised a multi-scale difference-of-Gaussians image representation (Lowe,

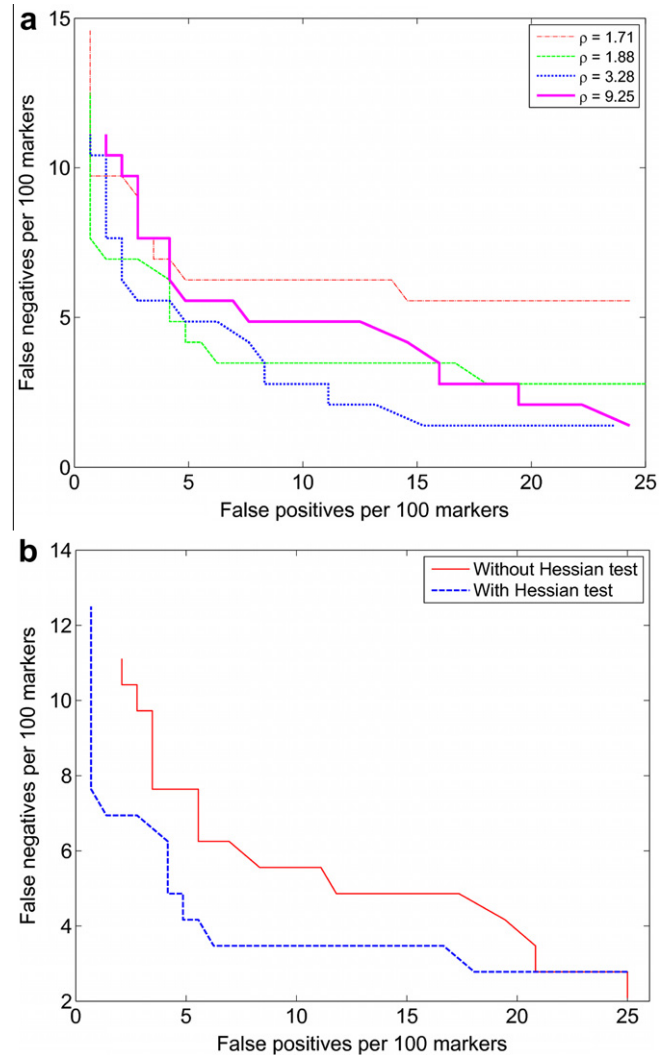


Fig.3. False negative and false positive rates per hundred markers obtained when detecting 10 nm markers in single-labelled micrographs. (a) Effect of varying thresholds τ and ρ_0 . (b) Effect of applying the Hessian eigenvalue ratio test with $\rho_0 = 1.88$ (The threshold τ ranges from 6.9 to 11.0 for the “without Hessian test” curve and from 5.5 to 11.0 for the “with Hessian test” curve).

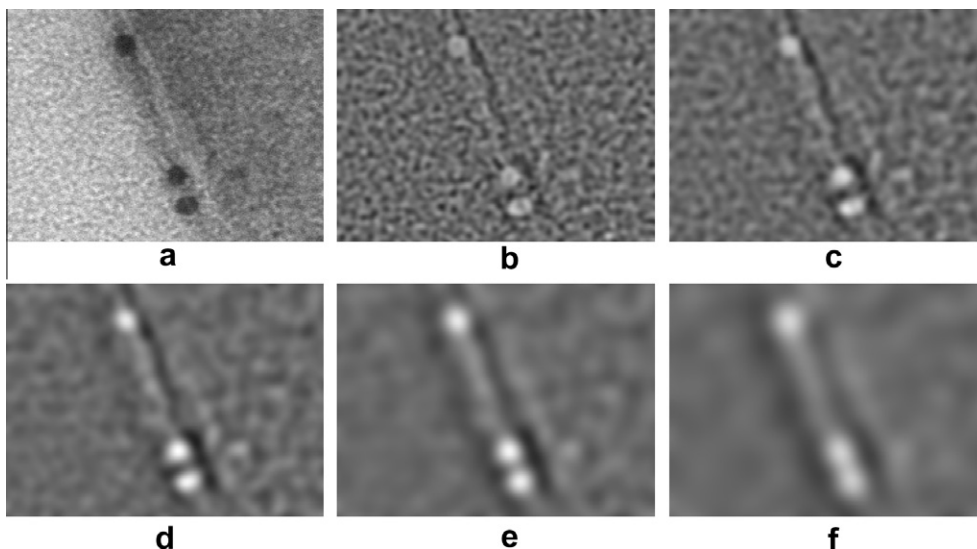


Fig.2. (a) Cropped image showing three immunogold markers located near a cell's external membrane. (b–f) DoG responses at filter scales $\sigma = 2.40$, $\sigma = 3.39$, $\sigma = 4.79$, $\sigma = 6.77$, and $\sigma = 9.58$, respectively. Gold particles were approximately 10 nm in size.

Table 1

Detection results with and without the Hessian eigenvalue ratio test for the micrographs labelled with 10 nm markers.

	True positives	False positives	False negatives
Without Hessian test	141	49	3
With Hessian test	138	6	6

Table 2

Detection results with and without the Hessian eigenvalue ratio test for the double labelled micrographs.

	True positives	False positives	False negatives
Without Hessian test	391	23	12
With Hessian test	390	16	13

2004). A set of local maxima indicating markers without severe spatial overlaps was selected as a candidate immunogold marker set. Analysis of Hessian matrices at candidate locations was then used to remove poor detections that occurred at strong edges or ridges. In the case of double-labelling, the method was modified to detect and classify differently sized markers.

2.2. Detecting candidate markers

Given an image $I(x, y)$, a linear scale-space (Lindeberg, 1994) is defined by convolution of the image with two-dimensional (2D) isotropic Gaussian kernels $G(\sigma, x, y)$ at scales $\sigma \geq 0$, where

$$G(\sigma, x, y) = \frac{1}{2\pi\sigma^2} \exp\left\{-\frac{x^2 + y^2}{2\sigma^2}\right\}$$

The Laplacian of Gaussian (LoG) filter is widely used for blob detection and is often approximated as a difference of Gaussians (DoG). The response of a DoG filter to an image $I(x, y)$ is given by

$$R(\sigma, x, y) = G(\sigma, x, y) * I(x, y) - G(\sqrt{2}\sigma, x, y) * I(x, y), \quad (1)$$

where $*$ denotes the convolution operation. The response of DoG filters at scales separated by a factor of $\sqrt{2}$ to three immunogold markers is shown in Fig. 2.

Consider an ideal immunogold marker image,

$$I(x, y) = \begin{cases} 1 & \text{if } (x - x_c)^2 + (y - y_c)^2 \leq r^2 \\ 0 & \text{otherwise} \end{cases} \quad (2)$$

where r is the marker's radius and (x_c, y_c) is its centre. The DoG response $R(\sigma, x, y)$ to this ideal marker has its maximum at $(0.60r, x_c, y_c)$.

Given user-provided values, r_{\min} and r_{\max} , for the minimum and maximum radii of immunogold markers to be detected, DoG filters were applied at equally separated scales at increments corresponding to a pixel increment in marker diameter. Specifically, scales used were $\sigma \in \{0.6(r_{\text{mid}} \pm j/2)\}$ where $r_{\text{mid}} = (r_{\min} + r_{\max})/2$, and j indexes the non-negative integers ranging from 0 to ceiling $(r_{\max} - r_{\min} + 1)$. Local maxima were detected by comparing responses to those at neighbouring pixels at the same scale and at adjacent scales. In other words, a particular image location and

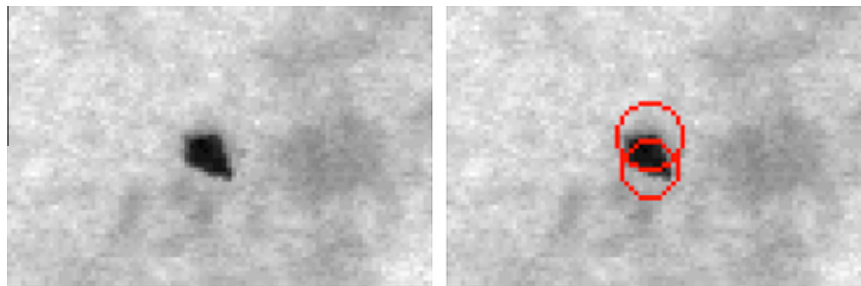


Fig. 4. An example of an artifact that gave rise to false positive errors ($\rho_0 = 1.88$, $\tau = 9.0$).

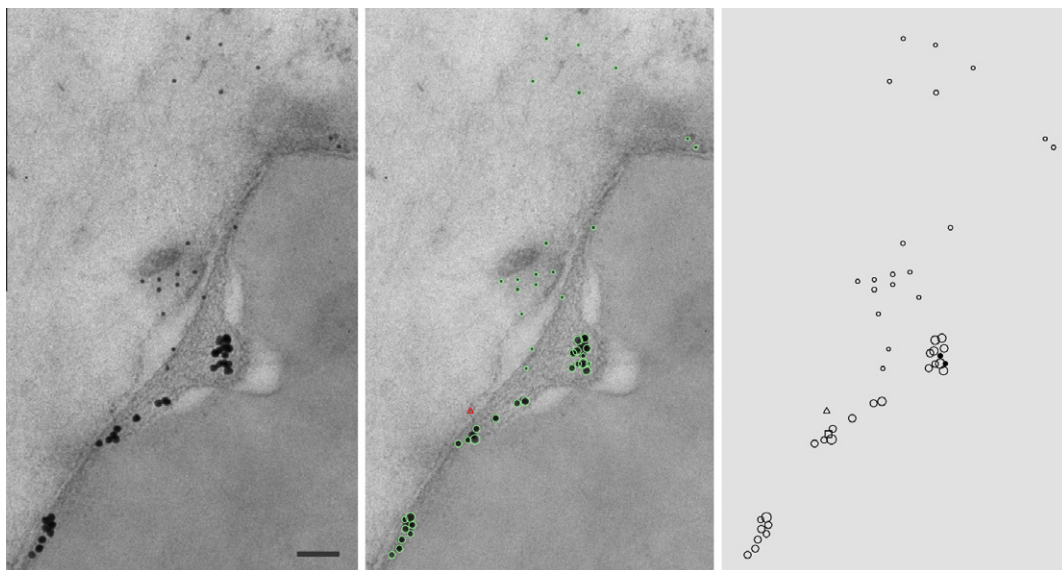


Fig. 5. Left: part of a double-labelled micrograph. Centre: detections overlaid on the micrograph: green circles denote true positives and the red triangle denotes a false positive. Right: detection and classification results with the one false negative denoted by a triangle and the two misclassified true positive detections denoted by filled circles ($\rho_0 = 1.88$, $\tau = 9.0$). Ultrathin section of a cell embedded in Lowicryl HM23. Bar, 100 nm. (For interpretation of the references to colour in this figure legend, the reader is referred to the web version of this article.)

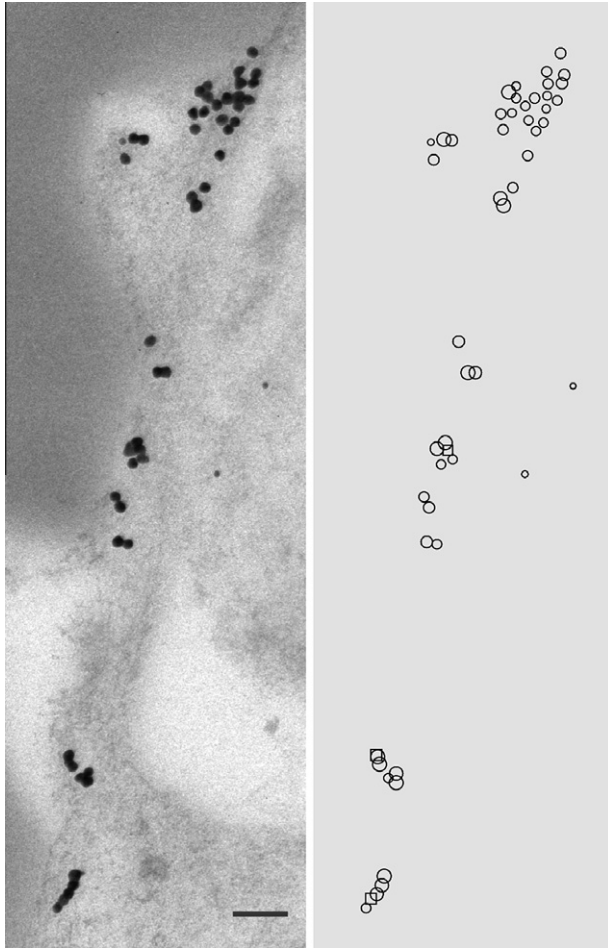


Fig. 6. Part of a double-labelled micrograph with immunogold marker detection and classification result ($\rho_0 = 1.88$, $\tau = 9.0$). There were three false negatives (denoted by squares). All detected markers in this image were correctly classified. Ultrathin section of a cell embedded in Lowicryl HM23. Bar, 100 nm.

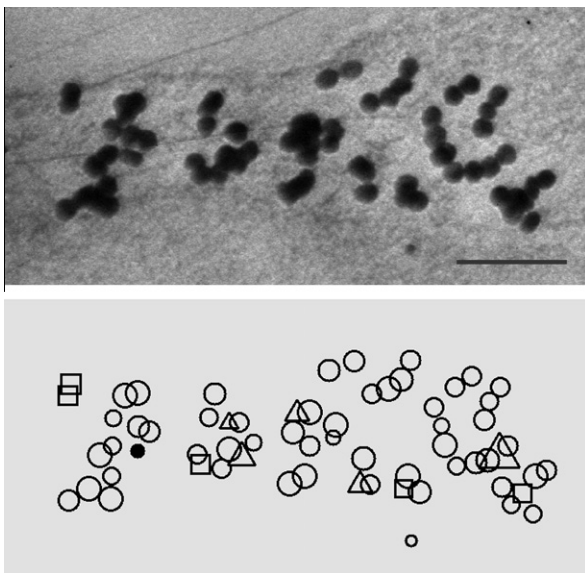


Fig. 7. Part of a double-labelled micrograph with immunogold marker detection and classification result ($\rho_0 = 1.88$, $\tau = 9.0$). There were five false positives (triangles) and five false negatives (squares). One of the true positive detections was misclassified (filled circle). Ultrathin section of cells embedded in Lowicryl HM23. Bar, 100 nm.

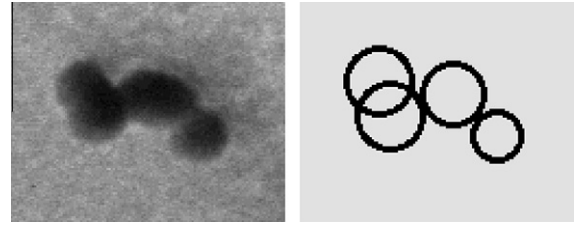


Fig. 8. Successful detection and classification of clustered markers ($\rho_0 = 1.88$, $\tau = 9.0$). Gold particles were approximately 20 nm in size.

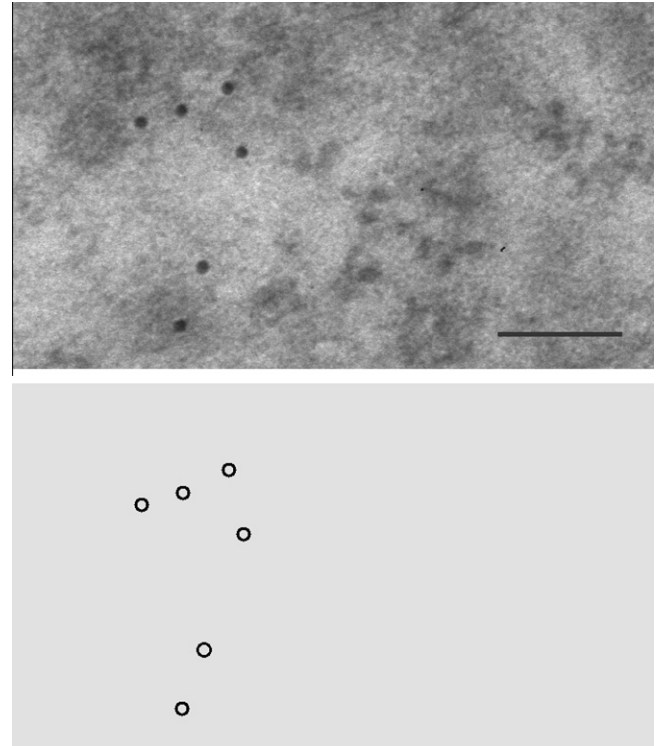


Fig. 9. Successful detection and classification in a strongly textured region ($\rho_0 = 1.88$, $\tau = 9.0$). Bar, 100 nm.

scale (σ, x, y) was at a local maximum if (i) the responses at the eight neighbouring pixels at that scale were lower, and (ii) the responses at that pixel location and at its eight neighbours were lower at both the next highest scale and at the next lowest scale.

Each local maximum indicates the image location and size of a possible immunogold marker. Specifically, a maximum at (σ_c, x_c, y_c) represents a marker hypothesis centred at location (x_c, y_c) with radius $\sigma_c/0.6$. The local maxima with responses larger than a threshold τ were sorted into a list ordered by response strength. Candidate markers were then selected from this list as follows. Each entry in the list was considered in turn from strongest to weakest. An entry was selected as a candidate marker if its centre, (x_c, y_c) , was not closer in the image to any previously selected candidate's centre than that candidate's radius.

2.3. Eliminating edges and ridges

The candidate gold markers detected so far are likely to include false positive detections due to strong DoG responses to highly contrasted edge-like and ridge-like features. While increasing the response threshold, τ , would remove these false detections, it would also remove many true detections. In order to eliminate edges and ridges with strong DoG response, a method based on

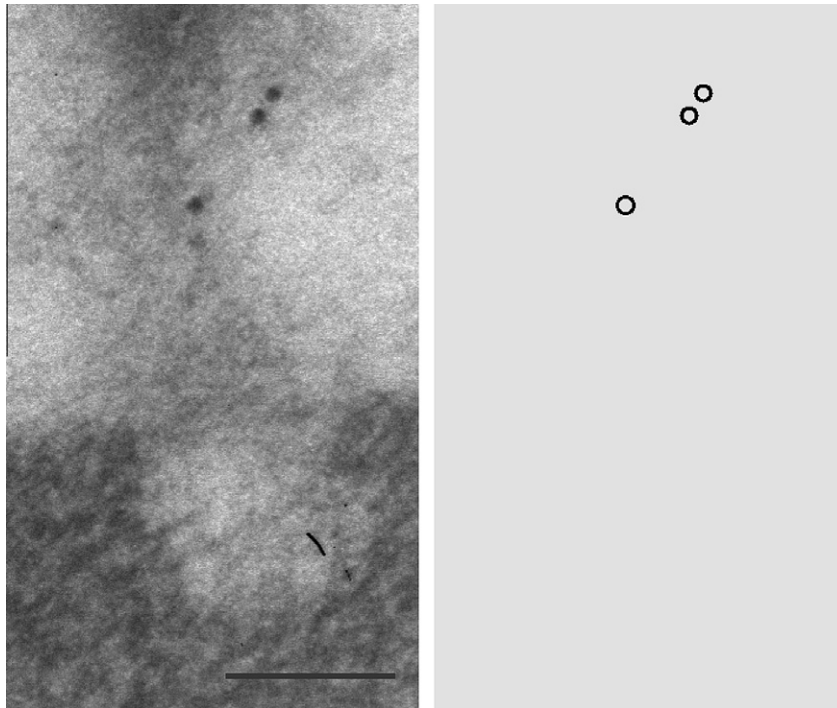


Fig.10. Successful detection and classification of low contrast markers in a strongly textured region ($\rho_0 = 1.88$, $\tau = 9.0$). Bar, 100 nm.

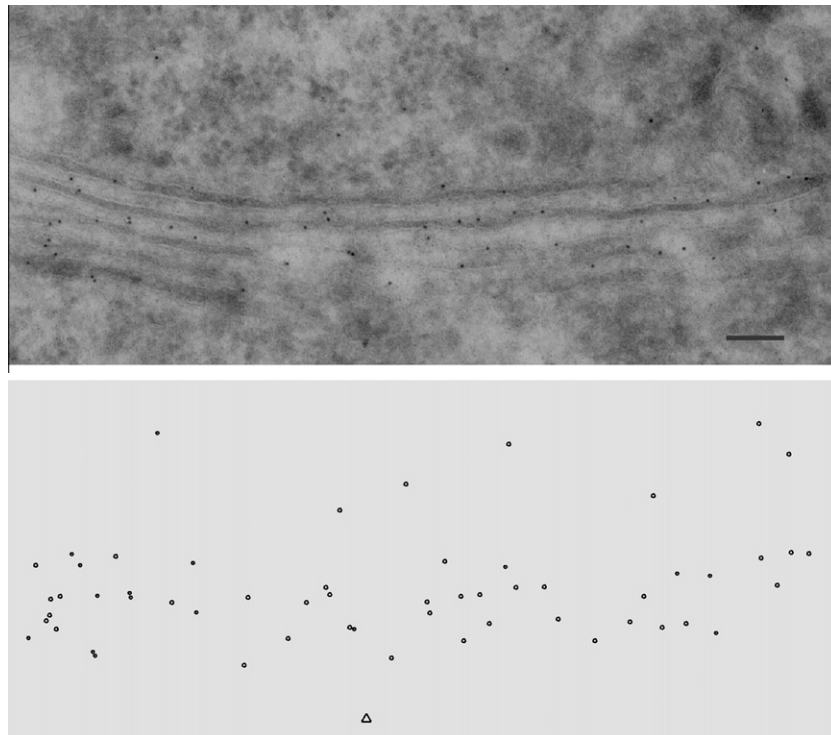


Fig.11. Part of a micrograph labelled using 8 nm markers and showing a Golgi stack. All markers were detected. There was one false positive, denoted as a triangle ($\rho_0 = 1.88$, $\tau = 9.0$). Thawed ultrathin cryosection. Bar, 100 nm.

analysis of the local Hessian was used. Consider a candidate gold marker at (σ', x', y') with locally maximal response $R(\sigma', x', y')$. The Hessian matrix at scale σ' and position (x', y') has the form

$$\mathbf{H} = \begin{bmatrix} R_{x'x'} & R_{x'y'} \\ R_{x'y'} & R_{y'y'} \end{bmatrix}. \quad (3)$$

The four second-order partial derivatives in \mathbf{H} were calculated based on finite difference approximations. Let α and β denote the eigenvalues of \mathbf{H} with $\alpha \geq \beta$. An ideal, radially symmetric marker image would have an eigenvalue ratio of $\rho = \alpha/\beta = 1.0$ whereas elongated structures such as edges and ridges will give larger values for this ratio. A large ratio indicates anisotropy. Since only the ratio is

relevant, eigenvalues need not be computed explicitly (Harris and Stephens, 1988). In order to check that the ratio ρ is greater than a threshold value ρ_0 , we only need to apply the following test (Lowe, 2004)

$$\frac{\text{Tr}^2(\mathbf{H})}{\text{Det}(\mathbf{H})} > \frac{(\rho_0 + 1)^2}{\rho_0}, \quad (4)$$

where Tr denotes the trace and Det the determinant of the matrix. This is because $(\rho + 1)^2/\rho$ strictly increases as ρ increases (provided that ρ is positive), and

$$\frac{\text{Tr}^2(\mathbf{H})}{\text{Det}(\mathbf{H})} = \frac{(\alpha + \beta)^2}{\alpha\beta} = \frac{(\rho + 1)^2}{\rho}, \quad (5)$$

If inequality (4) holds, the candidate marker (σ', x', y') is discarded. The threshold ρ_0 is a free parameter of the algorithm (see Section 3).

2.4. Marker detection and classification in double-labelled images

Double labelling, in which immunogold markers manufactured to be two different sizes are introduced, can be used to study spatial relationships between two different macromolecules. Fig. 5 shows part of a double-labelled micrograph. Running the marker detection algorithm independently at the two scale ranges corresponding to the two marker types can work poorly; large markers give rise to false detections at smaller scales not all of which can be successfully removed based on analysis of Hessian matrices. Instead, the method was used with a scale range wide enough to include both marker types and marker detections were subsequently classified into the two types.

When selecting candidate markers the rule for excluding markers that heavily overlapped other markers was modified. This was necessary because the markers' radii spanned a greater range in double-labelled images. Specifically, a tentative marker centred at (x_c, y_c) with radius r was not selected as a candidate marker if there existed a previously selected candidate marker centred at (x_i, y_i) with radius r_i such that $\sqrt{(x_c - x_i)^2 + (y_c - y_i)^2} < r_i$ or $\sqrt{(x_c - x_i)^2 + (y_c - y_i)^2} < r_c$. In other words, it was prohibited to have a marker's centre lying within another marker. Classification of immunogold marker type as *small* ('10 nm') or *large* ('20 nm') was performed based on thresholding of the estimated radii.

In the double-labelled images, immunogold markers often visually overlapped or appeared very close together. Even when correctly detected as candidates these cases can result in large values of ρ . Therefore the test in (4) was not applied to marker candidates whose centres were separated by a distance less than the sum of their diameters.

3. Results

Evaluation was performed on a set of five micrographs of sections that were single-labelled with 10 nm diameter immunogold markers, a set of five micrographs of sections that were double-labelled with 10 and 20 nm markers, and an additional set of three micrographs from sections single-labelled with 8 nm diameter markers. Micrographs were typically approximately 3000×3000 pixels. Ground-truth estimates of marker locations, radii, and type were obtained using an interactive annotation tool.

As an indication of processing time, a C# implementation running on a mid-range PC (1.8 GHz, 4 GB RAM, 64-bit processor) took 43 s to process the 3828×2276 pixel micrograph (from which the image in Fig. 7 was cropped) using DoG filters at 16 different scales ($r_{\min} = 6.5$, and $r_{\max} = 14$).

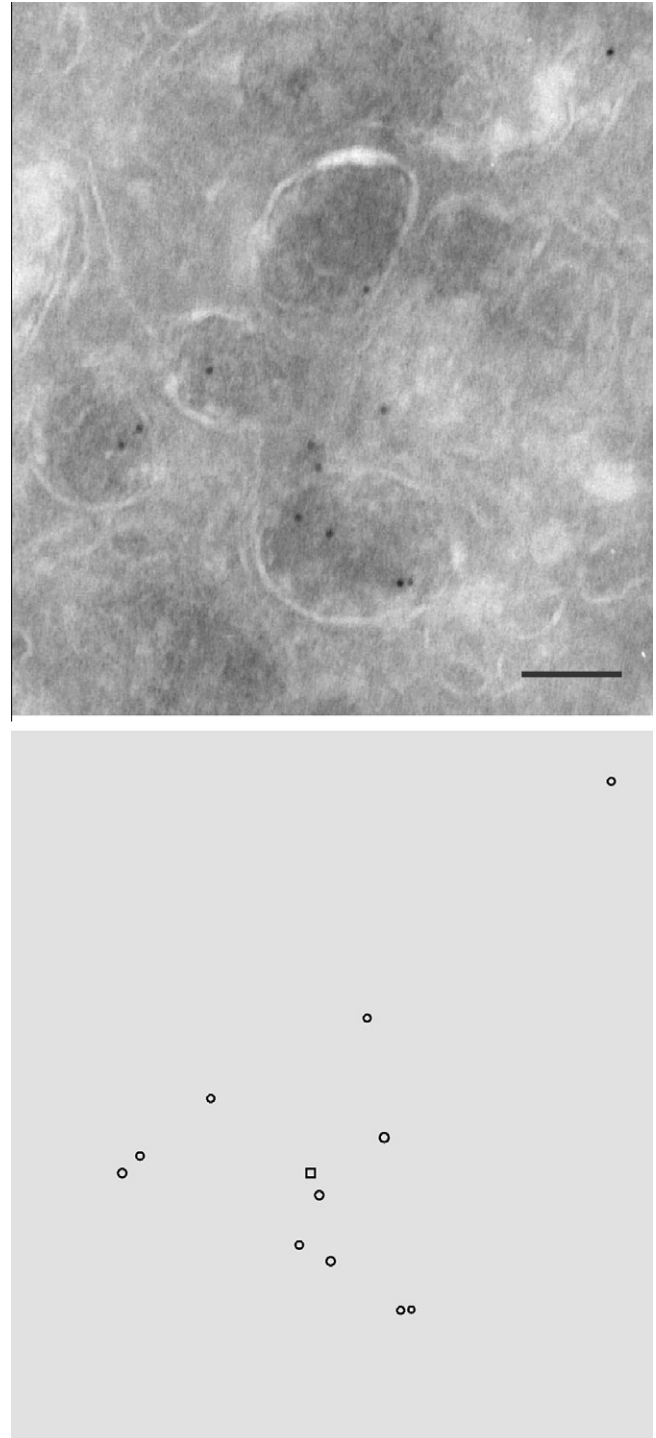


Fig. 12. Part of a micrograph labelled using 8 nm markers and showing lysosome. There was one false negative, denoted as a square. There were no false positives ($\rho_0 = 1.88$, $\tau = 9.0$). Thawed ultrathin cryosection. Bar, 100 nm.

3.1. Micrographs with single labelling (10 nm markers)

Fig. 3(a) displays plots of false-negative and false-positive rates per hundred true markers obtained from the set of images single-labelled with the 10 nm marker. Each curve was generated by varying the value of the DoG response threshold τ . A series of curves was generated by varying the eigenvalue ratio threshold ρ_0 . Four of these curves are shown in the Figure. When $\rho_0 = 1.88$ and $\tau = 6.9$, a rate of 4.9 false positives per 100 markers was

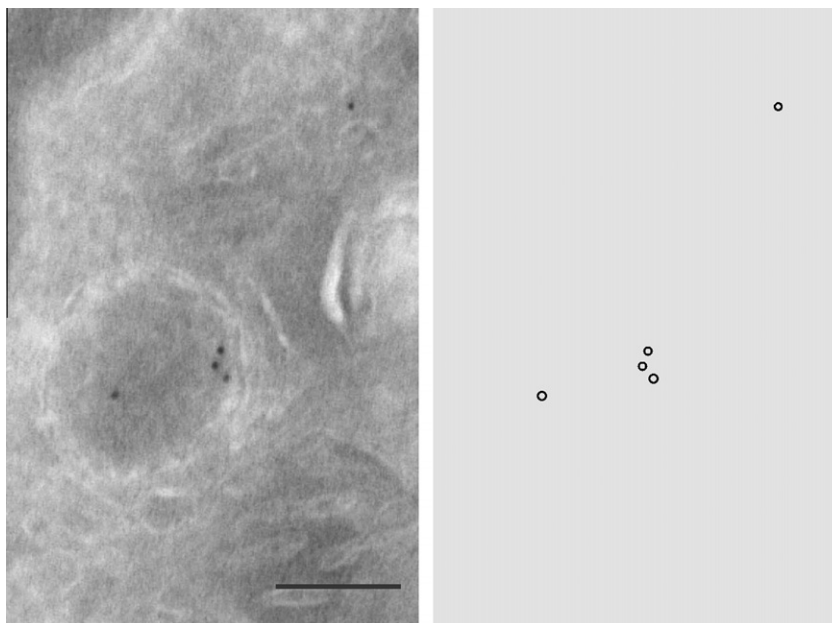


Fig. 13. Part of a micrograph labelled using 8 nm markers and showing lysosome. There were no detection errors ($\rho_0 = 1.88$, $\tau = 9.0$). Thawed ultrathin cryosection. Bar, 100 nm.

achieved at an approximately equal rate of 4.2 false negatives per 100 markers. Fig. 3(a) also shows that good results were obtained when $\rho_0 = 3.28$. Fig. 3(b) shows the effect of omitting the Hessian eigenvalue ratio test. Table 1 shows the numbers of true positives, false positives, and false negatives obtained on the single-labelled data set with $\rho_0 = 1.88$ and $\tau = 6.9$. The ratio test reduced the number of false positives significantly at the cost of a much smaller increase in the number of false negatives.

3.2. Micrographs with double labelling (10 and 20 nm markers)

Table 2 shows the numbers of true positives, false positives, and false negatives obtained on the double-labelled data set ($\rho_0 = 1.88$ and $\tau = 9.0$). Note that the Hessian eigenvalue ratio test was applied only to isolated marker candidates as described in Section 2.4. Applying the Hessian test to every candidate marker would have resulted in a large number of false negatives (113) because of a high incidence of heavily clustered markers in this data set.

Fig. 4 shows an unusual example that gave rise to false positive errors. It shows an artefact with an appearance similar to a gold marker. Two candidate markers were detected and because they were not spatially isolated, the Hessian test was not applied, resulting in false detections.

Figs. 5 and 6 show illustrative parts of micrographs along with detection and classification results. Results were good despite extreme clustering of markers. Fig. 7 shows a particularly problematic, unusually heavily clustered, small section of micrograph that accounted for a third of all detection errors in the double-labelled data set. Generally, the method performed well on clustered markers as shown in Fig. 8, for example. It also performed well in the presence of visual clutter caused by intracellular texture (see Fig. 9) and on poorly contrasted markers (see Fig. 10).

The radii distributions (histograms of the estimated radii using a bin size of 0.5 pixels) had a first local minimum at 8 pixels. This was the case for every image in the data set. Therefore, markers with estimated radii greater than 8 pixels were classified as *large* ('20 nm') and other markers as *small* ('10 nm'). There were 148 small markers and 242 large markers in the data set (according to the ground-truth labelling). Five large markers (2%) were misclassified as small. All small markers were correctly classified.

3.3. Micrographs with single labelling (8 nm markers)

Figs. 11–13 show illustrative parts of the three micrographs containing 8 nm markers. Fig. 11 shows markers located on and around a Golgi stack; the only detection error in this example is a single false positive. Figs. 12 and 13 include lysosomes; there is one error in Fig. 13, a false negative. These results provide further evidence that the detection algorithm is robust to changes in the scale of gold markers and to the presence of different organelles in the images.

4. Discussion and conclusions

The results presented here show that the method can detect immunogold markers with low false positive and false negative rates in both single-labelled and double-labelled micrographs. The method can be used to estimate marker radius and also to classify markers in double-labelled images with low misclassification error. Importantly, the clustered markers were generally well detected although heavy clustering gave rise to some errors. This feature makes this approach well suited to the analysis of gold labelling on ultrathin sections as well as in pre-embedding labelling. The fraction of false detections was also low, but false detections generally occurred in regions of highly contrasted clutter, some of which appeared to be artifacts of specimen preparation.

Workload involved in manual analysis of digitized immunoelectron micrographs depends on the exact nature of the task undertaken. However, as a rough indication, it took an expert (J. Lucocq) 43 s to count the 107 markers in the micrograph from which Fig. 7 was cropped. The method presented in this paper is fully automatic; large batches of images could be analysed without the need for user interaction. The processing time in our CPU implementation is dominated by the multi-scale DoG filtering step. This could be significantly accelerated by using a GPU implementation, for example (Kong et al., 2010).

This study now opens up the possibility of future work on automated gold particle counting. We now plan to focus on analysis of the spatial distribution of gold labelling and the associated molecules. Thus, once the marker locations have been identified, spatial statistics can be computed using point process models (or marked

point processes in the case of double labelling). A more ambitious goal is the automatic assignment of markers to intracellular compartments, requiring analysis of the cellular structure profiles that are apparent in the immunoelectron micrographs.

Acknowledgments

We thank Dr. Christian Gawden-Bone for supplying images of gold particles. R.W. and S.J.M. received support from an MRC/EPSRC/BBSRC Discipline Hopping Award to S.J.M. (Grant number G0902351).

References

- Brandt, S., Heikkonen, J., Engelhardt, P., 2001. Multiphase method for automatic alignment of transmission electron microscope images using markers. *Journal of Structural Biology* 133, 10–22.
- Harris, C., Stephens, M., 1988. A combined corner and edge detector. In: *Alvey Vision Conference*, 147–152.
- Kong, J., Dimitrov, M., Yang, Y., Liyanage, J., Cao, L., Staples, J., Mantor, M., Zhou, H., 2010. Accelerating MATLAB image processing toolbox functions on GPUs. In *Proceedings of the 3rd Workshop on General-Purpose Computation on Graphics Processing Units (GPGPU '10)* ACM, New York, 75–85.
- Lebonvallet, S., Mennesson, T., Bonnet, N., Girod, S., Plotkowski, C., Hinrasky, J., Puchelle, E., 1991. Semi-automatic quantitation of dense markers in cytochemistry. *Histochemistry and Cell Biology* 96, 245–250.
- Lindeberg, T., 1994. Scale-space theory: a basic tool for analyzing structures at different scales. *Journal of Applied Statistics* 21 (2), 225–270.
- Lowe, D.G., 2004. Distinctive image features from scale-invariant keypoints. *International Journal of Computer Vision* 60, 91–110.
- Lucocq, J.M., 1994. Quantitation of gold labelling and antigens in immunolabelled ultrathin sections. *Journal of Anatomy* 184, 1–13.
- Lucocq, J., 2008. Quantification of structures and gold labeling in transmission electron microscopy. *Methods in Cell Biology* 88, 59–82.
- Lucocq, J.M., Gawden-Bone, C., 2009. A stereological approach for estimation of cellular immunogold labeling and its spatial distribution in oriented sections using the rotator. *Journal of Histochemistry and Cytochemistry* 57, 709–719.
- Lucocq, J.M., Gawden-Bone, C., 2010. Quantitative assessment of specificity in immunoelectron microscopy. *Journal of Histochemistry and Cytochemistry* 58, 917–927.
- Lucocq, J.M., Habermann, A., Watt, S., Backer, J.M., Mayhew, T.M., Griffiths, G.A., 2004. A rapid method for assessing the distribution of gold labeling on thin sections. *Journal of Histochemistry and Cytochemistry* 52, 991–1000.
- Mayhew, T.M., 2007. Quantitative immunoelectron microscopy: alternative ways of assessing subcellular patterns of gold labeling. *Methods in Molecular Biology* 369, 309–329.
- Mayhew, T., Lucocq, J., Griffiths, G., 2002. Relative labelling index: a novel stereological approach to test for non-random immunogold labelling of organelles and membranes on transmission electron microscopy thin sections. *Journal of Microscopy* 205, 153–164.
- Monteiro-Leal, L.H., Troster, H., Campanati, L., Spring, H., Trendelenburg, M.F., 2003. Gold finder: a computer method for fast automatic double gold labeling detection, counting, and color overlay in electron microscopic images. *Journal of Structural Biology* 141, 228–239.
- Webster, P., Schwarz, H., Griffiths, G., 2008. Preparation of cells and tissues for immuno EM. *Methods in Cell Biology* 88, 45–58.